

New simulations of accreting DA white dwarfs: inferring accretion rates from the surface contamination

F. C. Wachlin¹, G. Vauclair^{2,3}, S. Vauclair^{2,3}, and L. G. Althaus¹

¹ Instituto de Astrofísica de La Plata (UNLP - CONICET). Facultad de Ciencias Astronómicas y Geofísicas. Universidad Nacional de La Plata, Argentina

e-mail: fcw@fcaglp.unlp.edu.ar

² Université de Toulouse, UPS-OMP, IRAP, France

³ CNRS, IRAP, 14 avenue Edouard Belin, 31400 Toulouse, France

December 20, 2021

ABSTRACT

Context. A non negligible fraction of white dwarf stars show the presence of heavy elements in their atmospheres. The most accepted explanation for this contamination is the accretion of material coming from tidally disrupted planetesimals, which form a debris disk around the star.

Aims. We provide a grid of models for hydrogen rich white dwarfs accreting heavy material. We sweep a 3D parameter space involving different effective temperatures, envelope's hydrogen content and accretion rates. The grid is appropriate for determining accretion rates in white dwarfs showing the presence of heavy elements.

Methods. Full evolutionary calculations of accreting white dwarfs were computed including all relevant physical processes, particularly the fingering (thermohaline) convection, a process neglected in most previous works, that has to be considered to obtain realistic estimations. Accretion is treated as a continuous process and bulk Earth composition is assumed for the accreted material.

Results. We obtain final (stationary or near stationary) and reliable abundances for a grid of models representing hydrogen rich white dwarfs of different effective temperatures and hydrogen contents, applied to various accretion rates.

Conclusions. Our results provide estimates of accretion rates, accounting for thermohaline mixing, to be used for further studies on evolved planetary systems.

Key words. (stars:) white dwarfs - stars: evolution - stars: abundances - stars: interiors - accretion, accretion disks - instabilities

1. Introduction

All the stars with masses lower than $8 M_{\odot}$, which constitute about 97% of the stellar population of the Galaxy, will end their evolution as white dwarfs (Iben et al. 1997). A large fraction of these stars host planets (Cassan et al. 2012). The fate of these planetary systems, when the stars evolve from the main-sequence up to the final white dwarf stage, has been the subject of considerable interest during the last decades (Debes & Sigurdsson 2002; Debes et al. 2012; Mustill et al. 2013; Veras et al. 2013; Frewen & Hansen 2014).

The infrared excess discovered around the DA white dwarf G29-38 (Zuckerman & Becklin 1987) and the photospheric contamination of white dwarfs by heavy elements are interpreted as the result of the disruption by tidal effects of planetesimals orbiting the white dwarf (Jura 2003). This scenario is confirmed by the observations of debris transiting the white dwarf WD1145+017 (Vanderburg et al. 2015) and the spectroscopic detection of planetesimal orbiting in the gaseous disk of SDSS1228+1040 (Manser et al. 2019). These observations show that small bodies in the planetary systems have survived during the host-star evolution. This implies that some planets must have survived as well. Such massive bodies are needed to perturb the orbits of the planetesimals and push them inside the white dwarf tidal radius where they disintegrate, as predicted by most scenarios of planetary systems evolution (Veras et al. 2013, 2014a,b, 2015a,b,c, 2016; Veras 2016).

The disrupted planetesimals feed the debris disk, and some of it is accreted onto the white dwarf, thereby polluting its atmosphere. Since the diffusion time-scale of the accreted heavy elements through the white dwarf external layers is much shorter than the evolutionary time-scale, the presence of heavy elements in the photosphere implies that the accretion process is ongoing. The study of polluted white dwarfs is accordingly a powerful way to study the chemical composition of the planetesimals and to better understand the various physical processes at work in the evolution of planetary systems.

The estimate of the accretion rates is an important input in this study. Most previous estimates of accretion rates were obtained by assuming that the accreted material, completely mixed in the surface convection zone, diffuses downwards on a diffusion time scale (Dupuis et al. 1992; Koester 2009; Farihi et al. 2012; Koester et al. 2014). Recently, Cunningham et al. (2019) explored the macroscopic diffusion induced by convective overshoot in DA white dwarfs by using three-dimensional (3D) radiation hydrodynamic simulations with the CO5BOLD code (Freytag et al. 2012). They found the mixed mass may increase by up to 2.5 dex, where such an increase of the mixed region leads to accretion rates which are a factor 2–5 larger.

Deal et al. (2013); Wachlin et al. (2017) and Bauer & Bildsten (2018, 2019) introduced in their computations the fingering convection process, which is indeed unavoidable in this context, since the accreted material, with a chemical composition mostly similar to that of the solar system

bodies (Swan et al. 2019) has a mean molecular weight larger than that of the white dwarf atmospheres. The inverse μ -gradient produces a double-diffusive instability, inducing extra-mixing of the accreted material (see for example Vauclair (2004); Stancliffe et al. (2007); Garaud (2011); Wachlin et al. (2011); Brown et al. (2013); Wachlin et al. (2014); Zemska et al. (2014)).

As shown by Deal et al. (2013) and confirmed by Wachlin et al. (2017) and Bauer & Bildsten (2018, 2019), this fingering convection has important consequences in the case of accreting DA white dwarfs, whereas it is absent or marginal in DB white dwarfs. In DA white dwarfs, the accretion rates needed to reproduce the photospheric abundances of heavy elements exceed by up to 2 orders of magnitude those estimated without this effect.

In this paper, we present the results of a series of numerical simulations of accretion onto DA white dwarfs. Our aim is to provide estimates of the accretion rates and of the photospheric chemical composition for a choice of heavy elements among the most often observed in polluted white dwarfs. Our simulations cover a large range of parameters for the effective temperature, hydrogen mass fraction and accretion rates. Due to computation time limitations, we have to restrict ourselves to study only one white dwarf’s mass. From these results, it is possible to infer an estimate of the accretion rate needed to reproduce the heavy element abundances deduced from the observations, knowing the effective temperature of the white dwarf. In section 2 we define the range of parameters covered by the simulations and describe how we obtain the initial models. Section 3 describes how the simulations have been performed. Section 4 gives the results of our simulations. A summary and a discussion of these results are given in section 5.

2. Initial models

To study the relation between the accretion rate and the resulting surface contamination of hydrogen-rich (DA) white dwarfs, we prepared a set of numerical experiments involving models of white dwarfs with different effective temperatures and different amounts of hydrogen content in their envelopes, (M_H). In particular, we choose the following effective temperatures: 6000K, 8000K, 10000K, 10500K, 11000K, 11500K, 12000K, 16000K, 20000K and 25000K and the following M_H values: $10^{-4}M_\odot$, $10^{-6}M_\odot$, $10^{-8}M_\odot$ and $10^{-10}M_\odot$. The value of M_H is particularly relevant since it impacts the depth of the transition zone between hydrogen-rich and helium-rich layers.

Our parameter space partially overlaps that of Bauer & Bildsten (2019), which spans the following ranges: $6000\text{K} < T_{\text{eff}} < 20000\text{K}$, $M_{\text{WD}}/M_\odot = 0.38, 0.60, 0.90$ and $\dot{M} = 10^4 \text{ g s}^{-1} - 10^{12} \text{ g s}^{-1}$, for a fixed hydrogen content in the envelope of $M_H = 10^{-6}M_{\text{wd}}$.

All initial setups are based on the $0.609 M_\odot$ ($Z = 0.01$) white dwarf model obtained by Renedo et al. (2010) from the full evolution of its progenitor star from the zero-age main sequence (ZAMS) to advanced stages on the thermally-pulsing asymptotic giant branch. To generate white dwarf configurations with smaller hydrogen contents than that dictated by progenitor evolution, we artificially reduced the hydrogen content by converting the excess of hydrogen into helium. This is enough for our purposes. In this work, we considered for each model four different accretion rates, namely $\log(\dot{M}) = 6, 8, 10, 12$, where \dot{M} is given in g.s^{-1} .

3. Numerical simulations

The white dwarf models used in this work were generated by the LPCODE stellar evolution code. This code has been tested and widely used in various stellar evolution contexts of low-mass and white dwarf stars (see Althaus et al. 2003, 2005; Salaris et al. 2013; Althaus et al. 2015; Miller Bertolami 2016; Silva Aguirre et al. 2020; Christensen-Dalsgaard et al. 2020, for details). An interesting point for the present work is that LPCODE computes the white dwarf evolution in a self-consistent way, including the modifications in the internal chemical distribution induced by dynamical convection, fingering convection, atomic diffusion, and nuclear reactions. Atomic diffusion has been implemented following Burger’s scheme (Burgers 1969) that provides the diffusion velocities in a multicomponent plasma under the influence of gravity, partial pressure, and induced electric fields. Partial ionization of metals is taken into account as it has important effects for the diffusion timescales.

We have introduced some changes in the code in order to simulate the accretion process. All computations were done by considering accretion as a continuous process. Accreted material was assumed to be uniformly distributed on the star’s surface (see below). We performed simulations for different accretion rates, ranging from 10^6 g/s to 10^{12} g/s . Metal abundances of accreted matter were set to mimic the composition of the bulk Earth (Allègre et al. 2001). Finally we used OPAL radiative opacities for different metallicities (Iglesias & Rogers 1996), complemented with the molecular opacities from (Alexander & Ferguson 1994) at low temperatures. Since bulk Earth composition was adopted for the accreted matter, a new set of opacity tables was generated from the OPAL website following this composition.

Considering that DA white dwarfs develop a convective envelope at effective temperatures lower than about 15000 K (Althaus & Benvenuto 1998; Chen & Hansen 2011; Bauer & Bildsten 2018), we implemented the accretion process in two different ways, depending on the presence or not of envelope convection¹. For those models with a convective envelope, the accreted material was instantaneously mixed in that region. This is a reasonable approximation since the convection timescale is much shorter than the evolutionary timescale (Van Grootel et al. 2012). Specifically, for a given integration timestep, we estimate the amount of material that is accreted according to the accretion rate, and this material is uniformly distributed in the whole convective zone. At higher effective temperatures, when convection is absent, a different criterion is instead required to distribute the accreted material in the very outer layers of the star. In this case, different approaches have been used in the past, either based on some arbitrary selection of the depth at which the accreted matter should be distributed homogeneously (Koester & Wilken 2006; Koester 2009) or by considerations that neglect the role of fingering convection instability (Gänsicke et al. 2012). It is worth noting that the deepening of the fingering convection instability eventually makes the choice

¹ Cunningham et al. (2019) found in their 3D radiation hydrodynamics simulations that a superficial convection zone develops at $T_{\text{eff}} \approx 18000 \text{ K}$. Due to numerical stability considerations, particularly related to the treatment of diffusion, 1D evolutionary codes may undergo convergence difficulties when the radially sampling extends too far out into the regions where convection first sets in, thus making it undetectable until the instability penetrates deeper at lower effective temperatures. Thus it is not surprising that 3D hydrodynamics simulations find convection to start earlier, at higher effective temperatures, than 1D codes.

Table 1. Adopted values for the set of parameters characterizing each model.

parameter	adopted values
$\log(M_{\text{H}}/M_{\odot})$	-4, -6, -8, -10
$\log \dot{M}$	6, 8, 10, 12^a
$T_{\text{eff}}/10^3\text{K}$	$6^b, 8^c, 10, 10.5, 11, 11.5, 12, 16, 20, 25$

Notes. Some combinations of parameters have been discarded because of the following reasons:

^(a) For maximum accretion rate, models with $\log(M_{\text{H}}/M_{\odot}) = -10$ and $T_{\text{eff}} \geq 10000\text{K}$ run out of our opacity tables because of the excess of metal accumulation at the surface.

^(b) Transforms into a DB white dwarf for $\log(M_{\text{H}}/M_{\odot}) = -8$ and -10 .

^(c) Same as (b) but for $\log(M_{\text{H}}/M_{\odot}) = -10$ models.

of that depth less critical. We performed additional calculations to verify this.

In this work, particular attention has been paid to the evolution of ^{16}O , ^{24}Mg , ^{28}Si , ^{40}Ca and ^{56}Fe . These elements are important since they have been detected in the photospheres of many white dwarfs (Zuckerman et al. 2003, 2007; Xu et al. 2014, 2019; Melis & Dufour 2017). Their presence in the final surface composition of our simulations allow us to link any given accretion rate with these surface abundances for each model, characterized by its effective temperature and amount of hydrogen.

The computation of energy transport was performed by using the double diffusion theory of Grossman et al. (1993) as described by Wachlin et al. (2011) Diffusion coefficients for fingering convection zones were obtained by adopting the prescription of Brown et al. (2013).

4. Results

In this section we describe the main results of our simulations, paying special attention not only to the final composition of the atmosphere but to the whole process that leads to the final state. Our models are characterized by three main parameters:

1. the amount of hydrogen contained in the envelope (M_{H}),
2. the effective temperature (T_{eff}),
3. the accretion rate (\dot{M}).

As mentioned before, four different models were considered, based on the amount of hydrogen that remains from the previous evolution. For each model we took initial configurations with ten different effective temperatures, ranging from 6000 K to 25000 K. Finally we subjected each model to four different accretion rates. The total number of simulations performed was 180. Table 1 shows the details of the parameters adopted for each set of models. Some sets of parameters could not be combined to perform the corresponding simulation because either the initial model was impossible to be generated as a hydrogen rich (DA) white dwarf, or because a thin hydrogen envelope combined with a large accretion rate produced surface compositions running out of the opacity tables.

According to its effective temperature, a model may present a convective envelope or not. This fact has some impact on the internal structure once a stationary state is reached. For instance, Fig. 1 shows the final chemical profile for two models with the largest amount of hydrogen ($10^{-4}M_{\odot}$), one having a convective envelope while the other not. Both models were obtained from an accretion rate of 10^{10} g/s . Convection mixes up the composition of the superficial layers in a very short timescale, thus

Table 2. Final iron surface abundances (in mass) for simulations turning on and off fingering convection. Three accretion rates were considered for initial models all having the same amount of hydrogen ($M_{\text{H}} = 10^{-4}M_{\odot}$) and effective temperature ($T_{\text{eff}} = 10000\text{ K}$). The last row shows the fractional difference between both models, with and without fingering convection.

	10^6 g/s	10^8 g/s	10^{10} g/s
including FC	0.80×10^{-7}	0.35×10^{-5}	0.90×10^{-4}
without FC	0.27×10^{-6}	0.27×10^{-4}	0.27×10^{-2}
without/with FC	3.4	7.7	30

leading to a homogeneous abundance of all elements in that region (shown in the figure as a horizontal line in the convective zone, CZ hereafter). Below the convective region and because of the inversion of the molecular weight (μ), a fingering convective zone (FCZ) sets in. As we will discuss later, the turbulent motions generated by this instability right below the bottom of the convective zone is responsible for transporting the heavy elements coming from the upper layers down into the deeper regions of the star. This figure clearly shows how the turbulence in the FCZ diminishes as we go deeper. Indeed, the slope of the chemical profile of the heavy elements in that region goes from almost horizontal (more homogeneously distributed material) near the bottom of the CZ, to very steep at the bottom of the FCZ, characterized by a smooth transition to the radiative transport regime. It is worth mentioning that since fingering convection is a more efficient process than element diffusion, larger accretion rates are needed to maintain a given surface contamination when fingering convection is taken into account, as shown by Deal et al. (2013) and Wachlin et al. (2017). We may show the incidence of taking fingering convection into account by comparing the final (stationary) surface abundance of one representative metal, namely iron, for simulations where we have turned on and off this process. Table 2 shows the results for these simulations performed using the same base model which has $M_{\text{H}} = 10^{-4}M_{\odot}$ and $T_{\text{eff}} = 10000\text{ K}$. From the table it becomes clear that fingering convection needs to be included when associating a surface contamination with the corresponding accretion rate. Neglecting this process results in superficial iron abundances which may differ by a factor up to 30 for these simulations.

Fig. 2 displays the temporal evolution of the photosphere's abundance of iron for an accretion rate of 10^6 g s^{-1} at three different effective temperatures. We note that for the hotter models, those with $T_{\text{eff}} = 8000\text{ K}$ and 10000 K , the abundance of iron reaches a stationary state well before the end of the simulation, which was set after 14000 yr of continuous accretion². However, at the lowest effective temperature, much more time is required to reach the stationary state (about 200000 yr)³. This is an expected behavior since as CZ becomes more massive as cooling proceeds, more time is needed to achieve the final (stationary) state. We mention that all of our simulations have been extended in order to reach a final state as close as possible to a stationary situation.

Fig. 3 reveals another feature of our simulations, namely, the contrast between the time required for the surface heavy ele-

² The end of these simulations was arbitrarily set to 14000 yr after confirming that a stationary state was reached.

³ Some simulations took about one week to run and still did not reach a stationary state. In those cases we report a lower value for the particular element in the corresponding table.

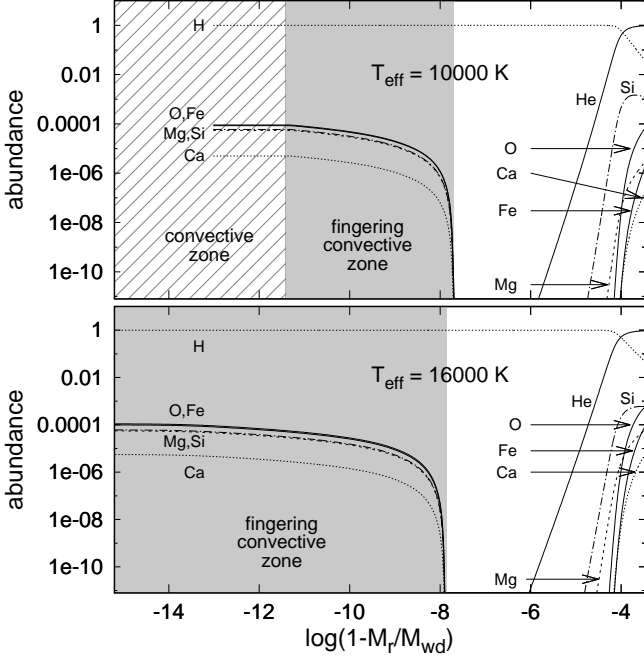


Fig. 1. Final chemical profile for two models with $M_H = 10^{-4} M_\odot$ but different effective temperatures. The accretion rate in both cases was of 10^{10} g s^{-1} .

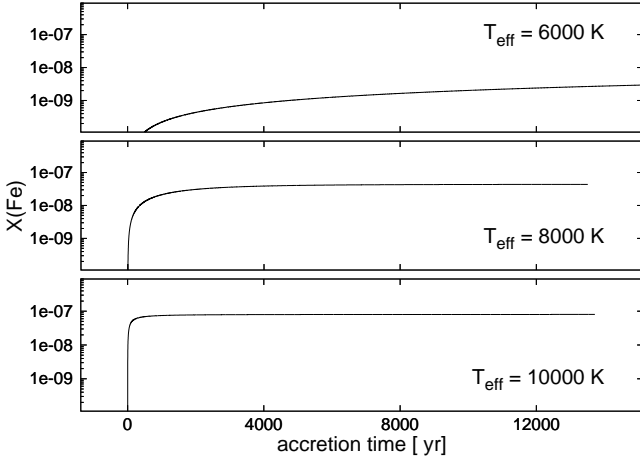


Fig. 2. Temporal evolution of the abundance (in mass) of iron for a continuous accretion rate of 10^6 g s^{-1} for white dwarf models with a hydrogen content of $10^{-4} M_\odot$ at three selected effective temperatures.

ments to reach the stationary state and the evolution of the FCZ. Indeed, while the abundance of iron, as well as that of the other heavy elements accreted (not shown), rapidly reach a stationary state, the bottom of the FCZ continues moving to deeper layers during white dwarf evolution. This is in contrast with the situation shown in Fig. 4 for the case of a smaller H envelope. Here, the inward advance of the bottom of the FCZ is halted by the H-He transition, where the inverse μ -gradient produced by the accretion is counteracted by the strong chemical gradient at the H-He interface. We note that in this case the evolution of the iron abundance is the same as that shown in Fig. 3, i.e. the stationary state is reached in a short time.

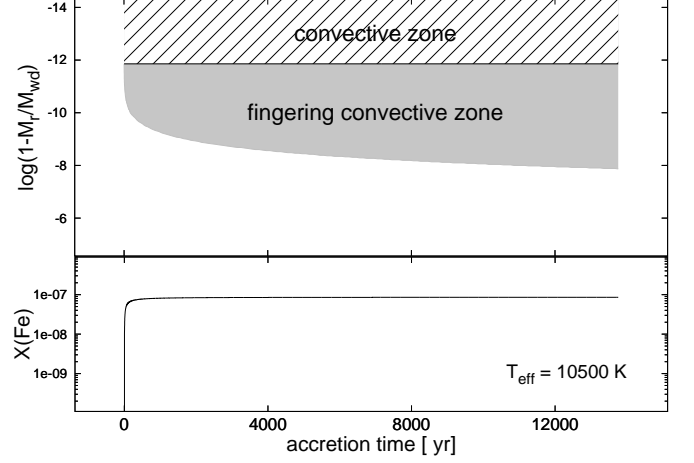


Fig. 3. Upper panel: time evolution of the convective and fingering convective zone during the accretion period for a model with $T_{\text{eff}} = 10500 \text{ K}$, $M_H = 10^{-4} M_\odot$ and accretion rate of 10^6 g s^{-1} . Bottom panel: evolution of the iron abundance (in mass) at the surface.

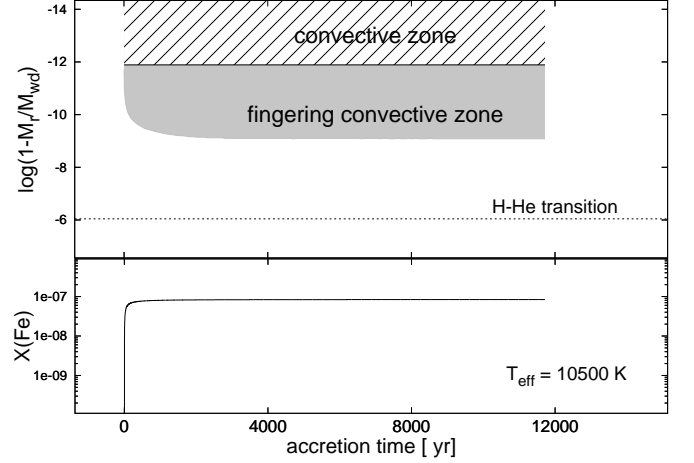


Fig. 4. Same as Fig. 3 but for a model with $M_H = 10^{-6} M_\odot$. A dotted horizontal line shows the depth where hydrogen abundance by mass falls below 0.5.

The impact of a thinner FCZ on the accumulation of heavy elements on the surface increases when the H-He transition is closer to the photosphere of the star. Fig. 5 illustrates how thin the FCZ becomes when the hydrogen mass in the envelope is reduced to $10^{-10} M_\odot$. In this case the bottom of the CZ penetrates more in the He-rich layers, lowering the contrast between the molecular weights inside the CZ and below. Because of the effect of the stabilizing μ -gradient produced by the increasing helium abundance as we go deeper, fingering convection barely shows up. Therefore, the expected presence of even a small amount of convective overshoot is likely to completely dominate such a small FCZ. The extension of the FCZ also depends on the accretion rate: the higher the accretion rate the wider the FCZ (not shown in the figure). In the case shown in Fig. 5, the abundance of iron increases by 15% with respect to the cases with a larger hydrogen envelope. This increase is not at all obvious in Fig. 5, but is more evident for higher accretion rates. Fig. 6 shows the dependence of the final iron abundances with the amount of hydrogen present in the envelope, for three different accretion rates.

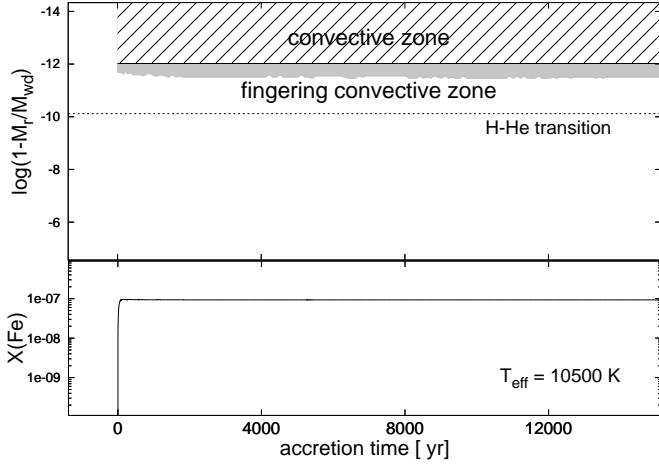


Fig. 5. Same as Figure 4 but for a model with $M_{\text{H}} = 10^{-10} M_{\odot}$.

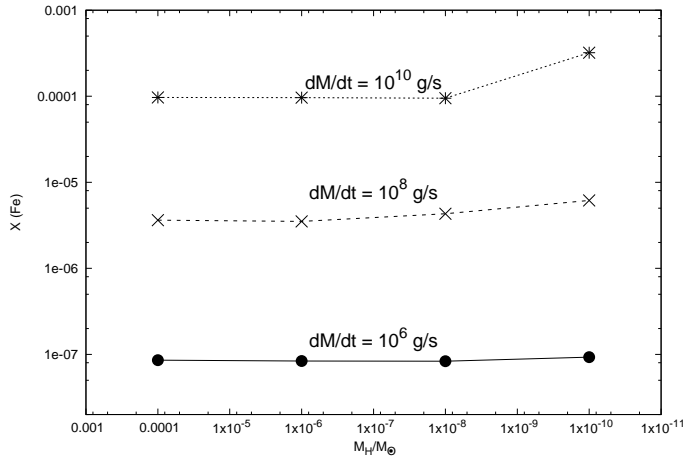


Fig. 6. Final abundances (in mass) of iron for envelopes of different amounts of hydrogen and different accretion rates.

The maximum difference with respect to the case with larger hydrogen envelope happens for an accretion rate of 10^{10} g s^{-1} , being the increase of 233%. In the intermediate case (10^8 g s^{-1}) the abundance increase is of 69%. Other simulations show a much higher accumulation of heavy elements when the FCZ becomes thin.

Models with a larger content of hydrogen have the H-He transition deeper and that may cause this region to be unreachable for the FCZ. In fact, all our simulations using models with $M_{\text{H}} = 10^{-4} M_{\odot}$ show that the bottom of the FCZ does not reach the H-He transition layers. Thus, the FCZ finds no obstacle to advance deeper as the simulation continues, although it slows down its pace as it penetrates into layers of increasing density. In contrast, the bottom of the convective zone (when the model has one) remains always at the same depth. Since the extension of the convective zone depends on the effective temperature, the level of accumulation of heavy elements on the surface will also depend on this parameter. Cooler models, with larger convective zones, rapidly spread the accreted material into this larger region, producing less contamination of the surface than in hotter white dwarfs. The evolution of the FCZ is faster for higher accretion rates, it also goes deeper carrying the heavy material further inside the star.

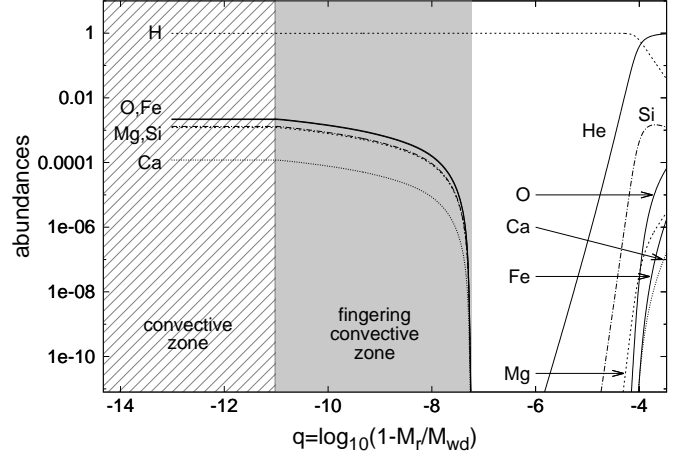


Fig. 7. Chemical profile of the final configuration of a model with $10^{-4} M_{\odot}$ of hydrogen, $T_{\text{eff}} = 10000 \text{ K}$ and accretion rate of 10^{12} g s^{-1} .

Fig. 7 shows the chemical profile at the end of the simulation for a model with $M_{\text{H}} = 10^{-4} M_{\odot}$, $T_{\text{eff}} = 10000 \text{ K}$ and maximum accretion rate (10^{12} g s^{-1}). The FCZ extends through a large region of the star (in a logarithmic scale in mass) but is still far from reaching the He-rich layers. Accreted heavy elements are homogeneously distributed throughout the convective zone but are less and less abundant as we advance deeper through the FCZ. The turbulence associated to the fingering convective instability is maximum near the bottom of the convective zone and diminishes downwards, tending gradually to zero. In our 1D computations, there is a somewhat sharp step in turbulence between dynamical and fingering convective zones, which would be smoother if 3D simulations of convection were taken into account (Freitag et al. 1996; Kupka et al. 2018; Cunningham et al. 2019). We did not add any 1D parametrization of overshoot or penetrative convection. A rapidly decreasing extra-mixing below the CZ would smoothen the local μ -gradient at the beginning of the simulations. Fingering convection would rapidly takeover, leading to similar final results. Detailed computations with various parameterizations of the bottom of the convective zones may be undertaken in the future.

In the case of thinner envelopes, the chemical evolution of accreting white dwarfs is quite different from the $M_{\text{H}} = 10^{-4} M_{\odot}$ case described before⁴. The main reason for such a difference is that now the turbulence from the upper layers is able to reach the H-He transition zone, something that does not happen for thicker envelopes.

We may start by describing our results for models with $M_{\text{H}} = 10^{-6} M_{\odot}$. For such a thin envelope, the FCZ which develops below the CZ expands until penetrating the transition zone where He becomes more abundant⁵. This encounter pre-

⁴ Cunningham et al. (2020) found observational evidence that approximately 20% of white dwarfs are expected to have a hydrogen content of $-14 < \log(M_{\text{H}}/M_{\text{wd}}) < -10$ whilst approximately 65% have $\log(M_{\text{H}}/M_{\text{wd}}) > -10$.

⁵ We found only two cases where no FCZ was formed. Both simulations correspond to the coolest models ($T_{\text{eff}} = 6000 \text{ K}$) and to the lower accretion rates (10^6 and 10^8 g s^{-1}). Two related facts are responsible for this result. First, the bottom of the convective zone deeply penetrates the H-He transition region reaching a stabilizing μ -gradient due to the increasing abundance of He as we go deeper. Second, the low accretion rate combined with a large CZ (which strongly dilutes the abundance of

vents the FCZ to go deeper, as it is stabilized by the normal μ -gradient due to the increasing amount of He. Thus, the heavy elements accumulated in the FCZ continue to progress further down by diffusion in a radiative medium, something that never happened in our previously described simulations of models with thicker envelopes, since the presence of heavy elements in a H-rich medium always triggered the fingering convection instability. Figure 8 shows such a situation for a model of $T_{\text{eff}} = 10500$ K and an accretion rate of 10^6 g s^{-1} . We expanded the abundance range to include very low values in order to show the contact between the bottom of the FCZ and the He tail, which stops the instability. We also note the dredge-up of He by the FCZ, which leads to the contamination of the surface by a very small amount in this case. As can be seen from Figure 8, the FCZ stops where the He/H abundance ratio reaches approximately 10^{-15} . The consecutive dredge-up of He would lead to an undetectable He abundance of $10^{-18.87}$ in the photosphere (see Table 5).

Larger He contamination is expected in the case of larger accretion rates, see Fig. 9. In this case, the FCZ is able to further penetrate the H-He transition region, with the consequent larger He enrichment of the outer layers. One can see from Fig. 9 that for an accretion rate of 10^{12} g s^{-1} , the FCZ stops where the He/H abundance ratio reaches approximately 10^{-4} . In this case, our simulation was interrupted before the steady state for the photospheric He abundance could be reached. The achieved lower limit for the abundance of He in the photosphere is $10^{-6.09}$ (see Table 5). The photospheric He abundance depends on both the hydrogen mass fraction and the accretion rate. In the cases where the hydrogen mass fraction could be independently derived and the accretion rate estimated from the observed heavy elements abundances, it should be possible to distinguish whether the photospheric helium has been accreted or dredged-up.

All the simulations with the highest accretion rates show this kind of behavior. Unfortunately the abundance of He on the surface takes much longer to reach a steady state than the accreted heavy elements, and we had to stop the simulations before that state was reached because of the excessive time required by the computation. We estimate that it takes of the order of 15000 yr of evolution to finally reach that steady state. Thus, our tabulated abundances of helium are only lower boundaries in most cases.

About 25% of the parameter space covered in this work was studied already by Bauer & Bildsten (2019) for a $\log(M_{\text{H}}/M_{\text{wd}}) = -6$ model. Table 3 compares both results, adding those obtained by Koester (2009). In all cases we show the diffusion calculations using the coefficients of Paquette et al. (1986). Some differences in the convective zone are apparent, arising from the differences between the Mixing Length Theory used by those works and the Grossman et al. (1993) convection theory implemented here.

Models with $M_{\text{H}} = 10^{-8} M_{\odot}$ share many of the main features of the $M_{\text{H}} = 10^{-6} M_{\odot}$ case. Dredge-up of helium is much more efficient now and consequently the contamination of the surface by helium is noticeably higher. The thinnest envelope models ($M_{\text{H}} = 10^{-10} M_{\odot}$) continue with the same tendency: more helium contamination of the surface and a FCZ advance stopped earlier by the more superficial H-He transition zone.

Figures 10 to 13 show how the surface contamination changes with the accretion rate for models of four different hydrogen envelopes. The details of the abundances at the end of each simulation are summarized in Tables 4 to 6.

heavy elements), lowers the difference between the molecular weights at the bottom of the CZ and the region immediately below it. The combination of these factors precludes the formation of the FCZ.

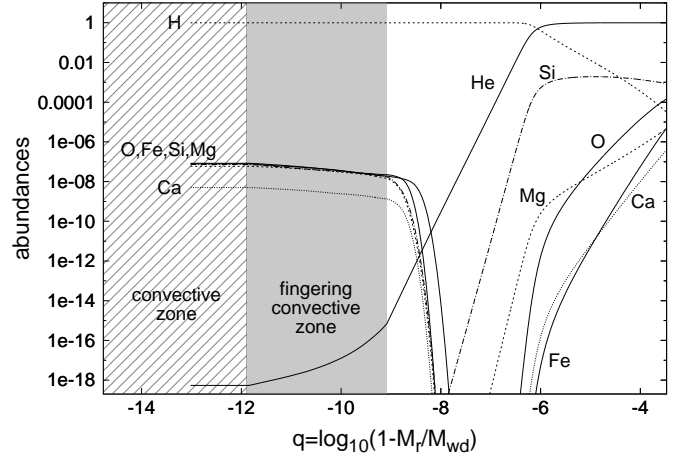


Fig. 8. Chemical profile of the final configuration of a model with $10^{-6} M_{\odot}$ of hydrogen, $T_{\text{eff}} = 10500$ K and accretion rate of 10^6 g s^{-1} .

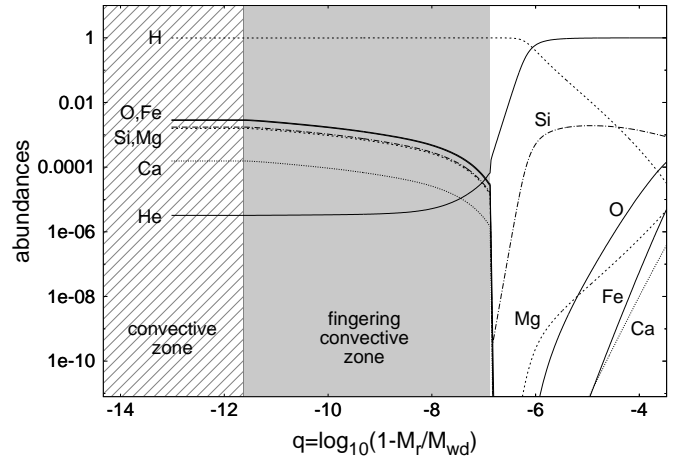


Fig. 9. Same as Fig. 8 but for a model with $10^{-6} M_{\odot}$ of hydrogen, $T_{\text{eff}} = 10500$ K but accretion rate of 10^{12} g s^{-1} .

Figure 11 includes the surface mass fractions for ^{40}Ca obtained by Bauer & Bildsten (2019). Although not strictly the same temperature, we include also their results for $T_{\text{eff}} = 15000$ K and 20500 K in our panels for 16000 K and 20000 K, respectively. They are some systematic differences for higher temperatures, where we obtain somewhat higher ^{40}Ca abundances than Bauer & Bildsten (2019). A better agreement is found for $T_{\text{eff}} \leq 10000$ K, although for $T_{\text{eff}} = 6000$ K we obtain smaller abundances for higher accretion rates. This difference is due to difficulties to reach the final steady state in our simulations because of the small timestep needed by our diffusion calculation (in these cases) to fulfill the required precision. Therefore, our results for $T_{\text{eff}} = 6000$ K and high accretion rates should be taken as lower boundaries. Figure 11 also includes for $T_{\text{eff}} = 11500$ K the steady state abundances for ^{16}O , ^{24}Mg , ^{28}Si , ^{40}Ca and ^{56}Fe provided by Bauer & Bildsten (2018) using the observed photospheric abundance of pollutants in G29–38. There is a good agreement for the abundances of ^{24}Mg , ^{28}Si and ^{56}Fe , whereas ^{16}O and ^{40}Ca show higher values (by about $\Delta[Z/X] = 0.44$) in Bauer & Bildsten (2018) work.

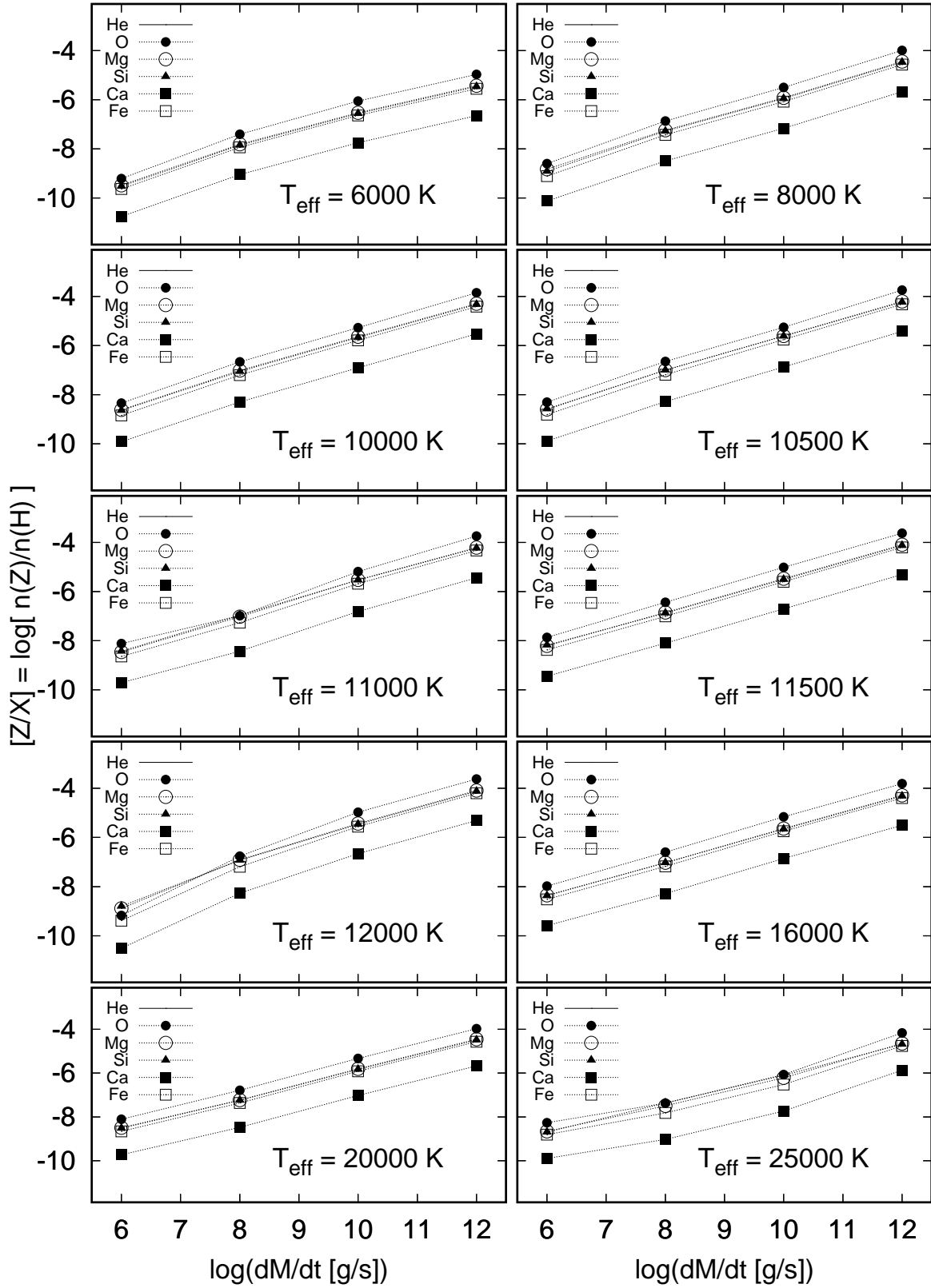


Fig. 10. Surface contamination against the accretion rate for models with $M_H = 10^{-4} M_\odot$. The contamination is given in terms of the abundance expressed in $[Z/H] = \log n(Z)/n(H)$.

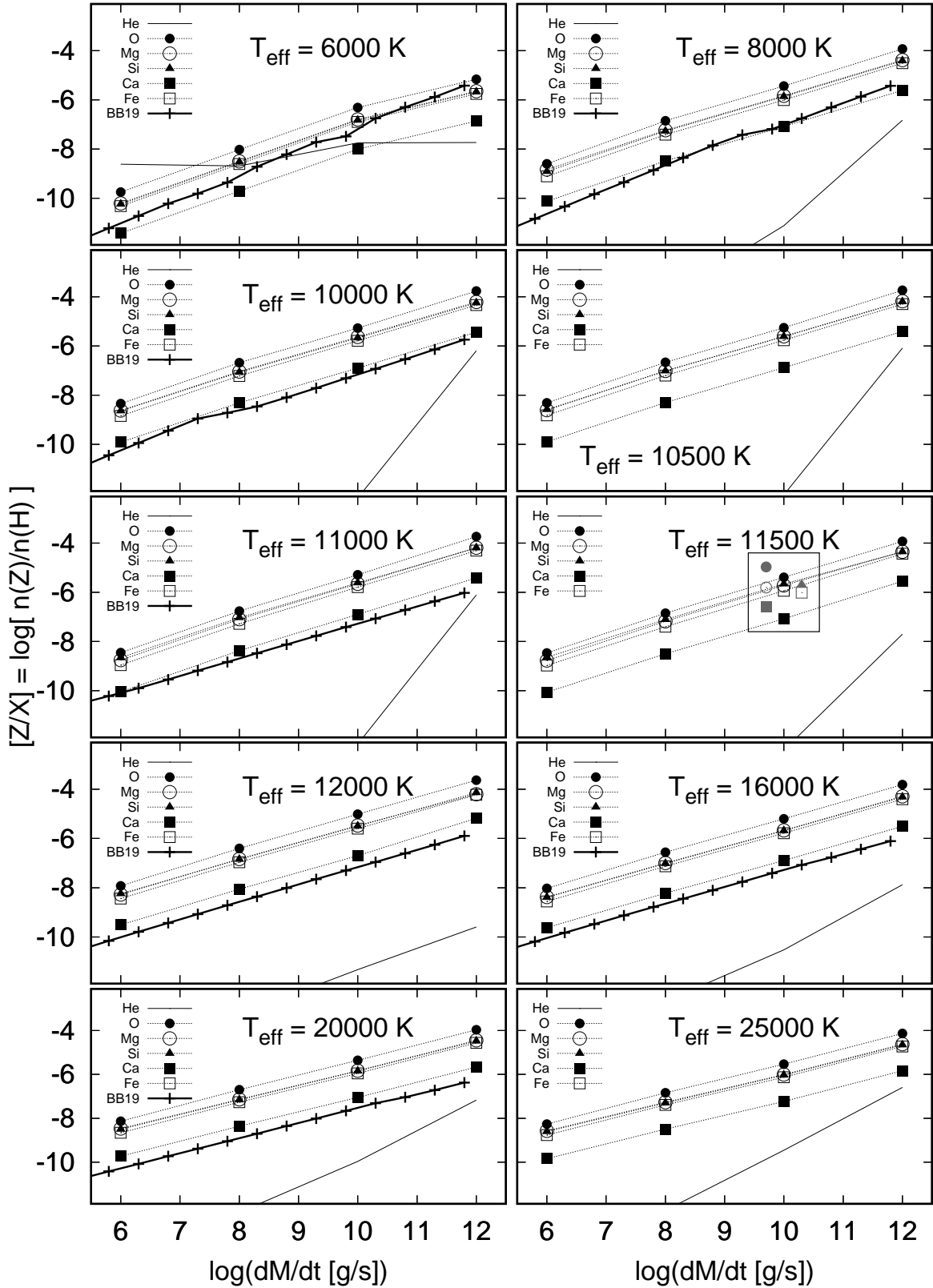


Fig. 11. Same as Figure 10 for models with $M_{\text{H}} = 10^{-6} M_{\odot}$. When possible, ^{40}Ca abundances obtained by Bauer & Bildsten (2019) have been added to the corresponding panel (labeled as BB19). For $T_{\text{eff}} = 11500 \text{ K}$, gray symbols (inside a box) represent the abundances obtained by Bauer & Bildsten (2018) for ^{16}O , ^{24}Mg , ^{28}Si , ^{40}Ca and ^{56}Fe using the observed photospheric abundance of pollutants in G29–38. All these isolated points correspond to an accretion rate of 10^{10} g s^{-1} but have been shifted a bit from that particular value for the sake of clarity.

Table 3. Comparison of Koester (2009), Bauer & Bildsten (2019) and our results for the mass of the surface convection zone and diffusion timescales for ^{40}Ca on a $0.6 M_{\odot}$ white dwarf.

T_{eff}	$\log(M_{\text{cvz}}/M_{\text{wd}})$			$\log g$		$\log(\tau_{\text{diff}}/\text{yr})$		
	Koester	BB19	here	BB19	here	Koester	BB19	here
6000 K	-7.722	-7.8094	-7.5803	8.0342	8.0594	4.2924	4.2449	4.4526
8000 K	-8.432	-8.9849	-9.7887	8.0272	8.0515	3.3303	3.4113	3.0643
10000 K	-10.738	-10.251	-11.456	8.0202	8.0447	1.9997	2.476	1.6092
11000 K	-12.715	-11.872	-12.714	8.0164	8.0413	0.4845	1.1984	0.2165
12000 K	-15.618	-14.698	-14.994	8.0127	8.0378	-1.6941	-1.0767	-1.5267

5. Summary and Discussion

We have presented a series of numerical simulations concerning the accretion of material produced by the disintegration of small rocky bodies onto DA white dwarfs. These simulations consider the effect of the double-diffusive instability, referred to as fingering convection. This instability is induced by the inverse μ -gradient resulting from the accretion of heavy material on the white dwarf outer layers. Our simulations are aimed at providing realistic estimates of the accretion rates, deduced from the observed heavy elements abundances in WD atmospheres, for a large range of effective temperatures, hydrogen-mass fractions and accretion rates. The results are presented in various graphs and tables, in such a way that the accretion rate may easily be deduced from the values of the heavy elements abundances. When fingering convection is properly considered, the resulting accretion rates may be up to several orders of magnitude larger than those estimated when ignoring its effect. For given values of the accretion rate and effective temperature, the accumulation of heavy elements in the WD atmospheres increases for decreasing hydrogen mass-fraction, since the fingering convection zone becomes thinner when the H/He transition zone is closer to the surface. In the cases of thin hydrogen mass-fraction and high accretion rates, the fingering convection may dredge-up some fraction of He from the H/He transition zone (see Tables 4 and 5). Such an effect produces DABZ type white dwarfs. We discuss below the various assumptions that have been adopted in our simulations.

The chemical composition of the accreted material is supposed to be similar to the Earth bulk composition. This is the case for most observed polluted DA white dwarfs (Swan et al. 2019). There are also evidences of other white dwarfs polluted by material with a variety of chemical composition (Gänsicke et al. 2012; Wilson et al. 2015; Melis & Dufour 2017) including water-rich and hydrated planetesimals (Farihi et al. 2013; Raddi et al. 2015; Hoskin et al. 2020) and volatile-rich planetesimals (Xu et al. 2017). Our simulations are not representative of such cases.

The accreted material is supposed to be mixed through the convection zone and through the fingering convection zone. Cunningham et al. (2021) find from their 3D radiation-hydrodynamics simulations that DA white dwarfs with effective temperature larger than 13000 K are unable to spread the accreted material horizontally on a time scale shorter than the diffusion time scale. However these diffusion time scales, estimated at the bottom of the convection zone, do not take into account the additional fingering convection zone. By considering fingering convection, diffusion happens deeper in the star and in a time scale which might be significantly longer. The absence of surface abundance variations in polluted DA white dwarfs (Debes & López-Morales 2008; Reach et al. 2009; Wilson et al. 2019) can be explained by 1) horizontal mixing being more efficient than predicted, 2) material being accreted in a generally

homogeneous surface distribution, or 3) observations not being sensitive enough to detect variations in abundance. Thus our assumption of homogeneously-mixed pollutants in turbulent zones is consistent with observations.

The mixing induced by the fingering convection is supposed to be a continuous process. The validity of this assumption has been called into question (Koester 2015). However, Brassard & Fontaine (2015) showed that in the case of a DA white dwarf with a hydrogen mass fraction of $M_{\text{H}} = 10^{-4}M_{\odot}$ and $T_{\text{eff}} = 11000$ K, the accretion of a C/O mixture at a rate of $9 \times 10^9 \text{ g s}^{-1}$ induces the fingering convection. Bauer & Bildsten (2018, 2019) have considered the case of accretion of bulk-Earth composition material and a range of accretion rates from 10^5 g s^{-1} to 10^{12} g s^{-1} . They find that fingering convection develops efficiently for accretion rates above approximately 10^6 g s^{-1} (see Bauer & Bildsten (2019) their figure 5). Multidimensional simulations accounting for convection and fingering mixing are clearly needed to probe how these two physical processes interact. The agreement between the results of Brassard & Fontaine (2015) and of Bauer & Bildsten (2018, 2019) and ours gives confidence in the way fingering convection is introduced in our simulations.

We hope that our results, with the figures and tables, will be useful to provide realistic estimates of the accretion rates, including the effect of fingering convection, to be used for further studies on evolved planetary systems.

Acknowledgements. We would like to thank an anonymous referee for the helpful comments, and constructive remarks on this manuscript. This work was supported by PICT-2017-0884 from ANPCyT, PIP 112-200801-00940 grant from CONICET, and grant G149 from University of La Plata. This research has made use of NASA Astrophysics Data System. F.C.W., G.V. and S.V. acknowledge financial support from "Programme National de Physique Stellaire (PNPS)" of CNRS/INSU, France.

References

- Alexander, D. R. & Ferguson, J. W. 1994, *ApJ*, 437, 879
Allègre, C., Manhès, G., & Lewin, É. 2001, *Earth and Planetary Science Letters*, 185, 49
Althaus, L. G. & Benvenuto, O. G. 1998, *MNRAS*, 296, 206
Althaus, L. G., Camisassa, M. E., Miller Bertolami, M. M., Córscico, A. H., & García-Berro, E. 2015, *A&A*, 576, A9
Althaus, L. G., Serenelli, A. M., Córscico, A. H., & Montgomery, M. H. 2003, *A&A*, 404, 593
Althaus, L. G., Serenelli, A. M., Panei, J. A., et al. 2005, *A&A*, 435, 631
Bauer, E. B. & Bildsten, L. 2018, *ApJ*, 859, L19
Bauer, E. B. & Bildsten, L. 2019, *ApJ*, 872, 96
Brassard, P. & Fontaine, G. 2015, in *Astronomical Society of the Pacific Conference Series*, Vol. 493, 19th European Workshop on White Dwarfs, ed. P. Dufour, P. Bergeron, & G. Fontaine, 121
Brown, J. M., Garaud, P., & Stellmach, S. 2013, *ApJ*, 768, 34
Burgers, J. M. 1969, *Flow Equations for Composite Gases*
Cassan, A., Kubas, D., Beaulieu, J. P., et al. 2012, *Nature*, 481, 167
Chen, E. Y. & Hansen, B. M. S. 2011, *MNRAS*, 413, 2827
Christensen-Dalsgaard, J., Silva Aguirre, V., Cassisi, S., et al. 2020, *A&A*, 635, A165
Cunningham, T., Tremblay, P.-E., Bauer, E. B., et al. 2021, *MNRAS*, 503, 1646

Table 4. Models with $M_{\text{H}} = 10^{-4} M_{\odot}$. Abundances are expressed in $[Z/H]$, where $[Z/H] = \log n(Z)/n(H)$ is the logarithmic number ratio of the abundance (in number) of element Z relative to the abundance of hydrogen (H). Lower values are marked by a > sign, when the stationary state was not achieved and the surface abundance of that element was still increasing.

		10^6 g s^{-1}	10^8 g s^{-1}	10^{10} g s^{-1}	10^{12} g s^{-1}
6000 K	He	-20.34	-19.67	-19.15	-19.25
	O	-9.16	-7.29	-5.88	-4.73
	Mg	-9.31	-7.62	-6.34	-5.16
	Si	-9.35	-7.66	-6.38	-5.21
	Ca	-10.63	-8.88	-7.56	-6.38
	Fe	-9.50	-7.76	-6.45	-5.30
8000 K	He	-29.63	-26.03	-25.35	-21.38
	O	-8.60	-6.86	-5.50	-3.99
	Mg	-8.83	-7.24	-5.92	-4.44
	Si	-8.91	-7.29	-5.95	-4.47
	Ca	-10.12	-8.49	-7.16	-5.67
	Fe	-9.11	-7.43	-6.07	-4.57
10000 K	He	-29.84	-25.00	-24.15	-21.93
	O	-8.34	-6.67	-5.28	-3.85
	Mg	-8.62	-7.02	-5.64	-4.29
	Si	-8.64	-7.05	-5.67	-4.33
	Ca	-9.91	-8.30	-6.90	-5.52
	Fe	-8.84	-7.21	-5.79	-4.41
10500 K	He	-29.61	-24.73	-23.87	-19.56
	O	-8.30	-6.65	-5.25	-3.74
	Mg	-8.60	-7.00	-5.61	-4.20
	Si	-8.58	-7.00	-5.62	-4.23
	Ca	-9.89	-8.28	-6.88	-5.42
	Fe	-8.81	-7.19	-5.76	-4.32
11000 K	He	-28.54	-24.79	-21.93	-23.69
	O	-8.12	-6.98	-5.18	-3.74
	Mg	-8.46	-7.03	-5.53	-4.21
	Si	-8.43	-6.96	-5.53	-4.24
	Ca	-9.72	-8.43	-6.81	-5.44
	Fe	-8.64	-7.27	-5.68	-4.33
11500 K	He	-27.43	-29.25	-27.12	-23.95
	O	-7.87	-6.44	-5.01	-3.62
	Mg	-8.21	-6.85	-5.48	-4.09
	Si	-8.18	-6.88	-5.51	-4.12
	Ca	-9.45	-8.10	-6.70	-5.31
	Fe	-8.37	-7.01	-5.60	-4.21
12000 K	He	-28.69	-29.32	-25.13	-24.59
	O	-9.18	-6.76	-4.97	-3.63
	Mg	-8.89	-6.91	-5.44	-4.09
	Si	-8.80	-6.92	-5.46	-4.12
	Ca	-10.51	-8.27	-6.66	-5.31
	Fe	-9.39	-7.19	-5.56	-4.20
16000 K	He	-25.29	-27.79	-23.90	-23.41
	O	-7.98	-6.60	-5.16	-3.81
	Mg	-8.35	-7.03	-5.63	-4.29
	Si	-8.37	-7.03	-5.66	-4.32
	Ca	-9.59	-8.28	-6.86	-5.50
	Fe	-8.52	-7.17	-5.75	-4.40
20000 K	He	-18.27	-29.02	-22.92	-22.45
	O	-8.11	-6.78	-5.33	-3.98
	Mg	-8.49	-7.23	-5.81	-4.46
	Si	-8.52	-7.24	-5.84	-4.49
	Ca	-9.73	-8.47	-7.03	-5.68
	Fe	-8.66	-7.36	-5.92	-4.57
25000 K	He	-22.46	-25.57	-21.90	-21.19
	O	-8.26	-7.37	-6.07	-4.16
	Mg	-8.66	-7.49	-6.21	-4.65
	Si	-8.69	-7.36	-6.10	-4.68
	Ca	-9.90	-9.03	-7.73	-5.86
	Fe	-8.81	-7.82	-6.52	-4.76

Cunningham, T., Tremblay, P.-E., Freytag, B., Ludwig, H.-G., & Koester, D. 2019, *MNRAS*, 488, 2503

Cunningham, T., Tremblay, P.-E., Gentile Fusillo, N. P., Hollands, M., & Cukanovaite, E. 2020, *MNRAS*, 492, 3540

Deal, M., Deheuvels, S., Vauclair, G., Vauclair, S., & Wachlin, F. C. 2013, *A&A*, 557, L12

Debes, J. H. & López-Morales, M. 2008, *ApJ*, 677, L43

Debes, J. H. & Sigurdsson, S. 2002, *ApJ*, 572, 556

Debes, J. H., Walsh, K. J., & Stark, C. 2012, *ApJ*, 747, 148

Dupuis, J., Fontaine, G., Pelletier, C., & Wesemael, F. 1992, *ApJS*, 82, 505

Farihi, J., Gänsicke, B. T., & Koester, D. 2013, *Science*, 342, 218

Farihi, J., Gänsicke, B. T., Wyatt, M. C., et al. 2012, *MNRAS*, 424, 464

Frewen, S. F. N. & Hansen, B. M. S. 2014, *MNRAS*, 439, 2442

Freytag, B., Ludwig, H.-G., & Steffen, M. 1996, *A&A*, 313, 497

Freytag, B., Steffen, M., Ludwig, H. G., et al. 2012, *Journal of Computational Physics*, 231, 919

Gänsicke, B. T., Koester, D., Farihi, J., et al. 2012, *MNRAS*, 424, 333

Garaud, P. 2011, *ApJ*, 728, L30

Grossman, S. A., Narayan, R., & Arnett, D. 1993, *ApJ*, 407, 284

Hoskin, M. J., Toloza, O., Gänsicke, B. T., et al. 2020, *MNRAS*, 499, 171

Iben, Icko, J., Ritossa, C., & García-Berro, E. 1997, *ApJ*, 489, 772

Iglesias, C. A. & Rogers, F. J. 1996, *ApJ*, 464, 943

Jura, M. 2003, *ApJ*, 584, L91

Koester, D. 2009, *A&A*, 498, 517

Koester, D. 2015, in *Astronomical Society of the Pacific Conference Series*, Vol. 493, 19th European Workshop on White Dwarfs, ed. P. Dufour, P. Bergeron, & G. Fontaine, 129

Koester, D., Gänsicke, B. T., & Farihi, J. 2014, *A&A*, 566, A34

Koester, D. & Wilken, D. 2006, *A&A*, 453, 1051

Kupka, F., Zaussinger, F., & Montgomery, M. H. 2018, *MNRAS*, 474, 4660

Manser, C. J., Gänsicke, B. T., Eggl, S., et al. 2019, *Science*, 364, 66

Melis, C. & Dufour, P. 2017, *ApJ*, 834, 1

Miller Bertolami, M. M. 2016, *A&A*, 588, A25

Mustill, A. J., Villaver, E., Veras, D., Bonsor, A., & Wyatt, M. C. 2013, in *European Physical Journal Web of Conferences*, Vol. 47, *European Physical Journal Web of Conferences*, 06008

Paquette, C., Pelletier, C., Fontaine, G., & Michaud, G. 1986, *ApJS*, 61, 177

Raddi, R., Gänsicke, B. T., Koester, D., et al. 2015, *MNRAS*, 450, 2083

Reach, W. T., Lisse, C., von Hippel, T., & Mullally, F. 2009, *ApJ*, 693, 697

Renedo, I., Althaus, L. G., Miller Bertolami, M. M., et al. 2010, *ApJ*, 717, 183

Salaris, M., Althaus, L. G., & García-Berro, E. 2013, *A&A*, 555, A96

Silva Aguirre, V., Christensen-Dalsgaard, J., Cassisi, S., et al. 2020, *A&A*, 635, A164

Stancifffe, R. J., Glebbeek, E., Izzard, R. G., & Pols, O. R. 2007, *A&A*, 464, L57

Swan, A., Farihi, J., Koester, D., et al. 2019, *MNRAS*, 490, 202

Van Grootel, V., Dupret, M. A., Fontaine, G., et al. 2012, *A&A*, 539, A87

Vanderburg, A., Johnson, J. A., Rappaport, S., et al. 2015, *Nature*, 526, 546

Vauclair, S. 2004, *ApJ*, 605, 874

Veras, D. 2016, *Royal Society Open Science*, 3, 150571

Veras, D., Eggl, S., & Gänsicke, B. T. 2015a, *MNRAS*, 452, 1945

Veras, D., Eggl, S., & Gänsicke, B. T. 2015b, *MNRAS*, 451, 2814

Veras, D., Jacobson, S. A., & Gänsicke, B. T. 2014a, *MNRAS*, 445, 2794

Veras, D., Leinhardt, Z. M., Bonsor, A., & Gänsicke, B. T. 2014b, *MNRAS*, 445, 2244

Veras, D., Leinhardt, Z. M., Eggl, S., & Gänsicke, B. T. 2015c, *MNRAS*, 451, 3453

Veras, D., Mustill, A. J., Bonsor, A., & Wyatt, M. C. 2013, *MNRAS*, 431, 1686

Veras, D., Mustill, A. J., Gänsicke, B. T., et al. 2016, *MNRAS*, 458, 3942

Wachlin, F. C., Miller Bertolami, M. M., & Althaus, L. G. 2011, *A&A*, 533, A139

Wachlin, F. C., Vauclair, G., Vauclair, S., & Althaus, L. G. 2017, *A&A*, 601, A13

Wachlin, F. C., Vauclair, S., & Althaus, L. G. 2014, *A&A*, 570, A58

Wilson, D. J., Gänsicke, B. T., Koester, D., et al. 2019, *MNRAS*, 483, 2941

Wilson, D. J., Gänsicke, B. T., Koester, D., et al. 2015, *MNRAS*, 451, 3237

Xu, S., Dufour, P., Klein, B., et al. 2019, *AJ*, 158, 242

Xu, S., Jura, M., Koester, D., Klein, B., & Zuckerman, B. 2014, *ApJ*, 783, 79

Xu, S., Zuckerman, B., Dufour, P., et al. 2017, *ApJ*, 836, L7

Zemskova, V., Garaud, P., Deal, M., & Vauclair, S. 2014, *ApJ*, 795, 118

Zuckerman, B. & Becklin, E. E. 1987, *Nature*, 330, 138

Zuckerman, B., Koester, D., Melis, C., Hansen, B. M., & Jura, M. 2007, *ApJ*, 671, 872

Zuckerman, B., Koester, D., Reid, I. N., & Hünsch, M. 2003, *ApJ*, 596, 477

Table 5. Same as Table 4 for models with $M_{\text{H}} = 10^{-6}M_{\odot}$

		10^6 g s^{-1}	10^8 g s^{-1}	10^{10} g s^{-1}	10^{12} g s^{-1}
6000 K	He	-8.50	-8.33	-7.75	> -7.74
	O	-9.34	-7.51	-6.31	-5.16
	Mg	-9.71	-7.94	-6.79	-5.65
	Si	-9.74	-7.97	-6.83	-5.68
	Ca	-10.95	-9.15	-8.01	-6.86
	Fe	-9.83	-8.04	-6.90	-5.75
8000 K	He	-17.79	-14.07	-11.12	> -6.83
	O	-8.61	-6.85	-5.44	-3.92
	Mg	-8.83	-7.23	-5.83	-4.38
	Si	-8.91	-7.27	-5.87	-4.41
	Ca	-10.13	-8.48	-7.09	-5.61
	Fe	-9.11	-7.42	-6.00	-4.51
10000 K	He	-18.86	-14.71	-12.18	> -6.20
	O	-8.34	-6.68	-5.27	-3.76
	Mg	-8.62	-7.04	-5.63	-4.21
	Si	-8.64	-7.07	-5.67	-4.25
	Ca	-9.91	-8.31	-6.90	-5.44
	Fe	-8.84	-7.22	-5.79	-4.33
10500 K	He	-18.87	-14.64	-12.05	> -6.09
	O	-8.31	-6.66	-5.26	-3.73
	Mg	-8.61	-7.02	-5.61	-4.18
	Si	-8.59	-7.02	-5.62	-4.20
	Ca	-9.90	-8.30	-6.88	-5.41
	Fe	-8.82	-7.20	-5.76	-4.30
11000 K	He	-19.49	-14.30	-12.17	> -6.11
	O	-8.45	-6.77	-5.28	-3.73
	Mg	-8.76	-7.10	-5.65	-4.19
	Si	-8.66	-7.03	-5.62	-4.20
	Ca	-10.05	-8.38	-6.90	-5.41
	Fe	-8.96	-7.29	-5.79	-4.30
11500 K	He	-19.51	-14.52	-12.42	> -7.70
	O	-8.47	-6.85	-5.39	-3.93
	Mg	-8.77	-7.18	-5.72	-4.35
	Si	-8.64	-7.11	-5.66	-4.35
	Ca	-10.06	-8.50	-7.08	-5.54
	Fe	-8.97	-7.40	-5.94	-4.43
12000 K	He	-19.30	-13.16	-11.33	> -8.20
	O	-7.93	-6.40	-5.01	-3.61
	Mg	-8.28	-6.83	-5.48	-4.09
	Si	-8.24	-6.85	-5.50	-4.11
	Ca	-9.51	-8.05	-6.70	-5.31
	Fe	-8.44	-6.97	-5.60	-4.20
16000 K	He	-18.27	-12.62	-10.52	> -7.88
	O	-8.03	-6.56	-5.20	-3.81
	Mg	-8.38	-7.00	-5.67	-4.29
	Si	-8.39	-7.02	-5.69	-4.32
	Ca	-9.62	-8.22	-6.89	-5.50
	Fe	-8.56	-7.13	-5.79	-4.40
20000 K	He	-16.40	-12.29	> -9.96	> -7.17
	O	-8.13	-6.70	-5.36	-3.96
	Mg	-8.47	-7.14	-5.83	-4.45
	Si	-8.50	-7.16	-5.85	-4.48
	Ca	-9.72	-8.36	-7.05	-5.66
	Fe	-8.66	-7.26	-5.95	-4.56
25000 K	He	-16.15	-12.20	> -9.46	> -6.59
	O	-8.26	-6.83	-5.53	-4.14
	Mg	-8.57	-7.27	-6.01	-4.62
	Si	-8.61	-7.30	-6.03	-4.65
	Ca	-9.84	-8.50	-7.23	-5.83
	Fe	-8.76	-7.39	-6.13	-4.73

Table 6. Same as Table 4 for models with $M_{\text{H}} = 10^{-8}M_{\odot}$

		10^6 g s^{-1}	10^8 g s^{-1}	10^{10} g s^{-1}	10^{12} g s^{-1}
8000 K	He	-8.65	-6.63	-4.81	> -2.70
	O	-8.62	-6.72	-5.45	-3.99
	Mg	-8.81	-7.03	-5.89	-4.44
	Si	-8.92	-7.07	-5.92	-4.48
	Ca	-10.12	-8.30	-7.15	-5.68
	Fe	-9.10	-7.27	-6.04	-4.59
10000 K	He	-10.24	-6.81	-4.78	> -3.96
	O	-8.35	-6.60	-5.26	-3.92
	Mg	-8.62	-6.89	-5.64	-4.37
	Si	-8.65	-6.93	-5.68	-4.40
	Ca	-9.91	-8.19	-6.91	-5.59
	Fe	-8.85	-7.12	-5.79	-4.49
10500 K	He	-10.27	-6.77	-4.77	> -2.60
	O	-8.32	-6.59	-5.25	-3.78
	Mg	-8.61	-6.89	-5.62	-4.23
	Si	-8.60	-6.90	-5.64	-4.26
	Ca	-9.90	-8.19	-6.89	-5.46
	Fe	-8.83	-7.11	-5.77	-4.35
11000 K	He	-10.54	-6.82	-4.80	> -2.62
	O	-8.32	-6.61	-5.20	-3.72
	Mg	-8.65	-6.94	-5.61	-4.19
	Si	-8.59	-6.90	-5.59	-4.20
	Ca	-9.94	-8.25	-6.90	-5.42
	Fe	-8.86	-7.16	-5.77	-4.31
11500 K	He	-10.08	-6.51	-4.71	> -2.70
	O	-8.07	-6.44	-5.11	-3.73
	Mg	-8.41	-6.81	-5.55	-4.18
	Si	-8.37	-6.82	-5.57	-4.20
	Ca	-9.66	-8.06	-6.81	-5.43
	Fe	-8.58	-6.99	-5.70	-4.32
12000 K	He	-9.73	-6.34	-4.64	> -3.60
	O	-7.92	-6.33	-5.00	-3.64
	Mg	-8.25	-6.72	-5.47	-4.12
	Si	-8.22	-6.74	-5.49	-4.15
	Ca	-9.49	-7.94	-6.70	-5.33
	Fe	-8.42	-6.87	-5.59	-4.23
16000 K	He	-9.11	-6.09	-4.61	> -3.74
	O	-8.01	-6.44	-5.18	-4.75
	Mg	-8.33	-6.86	-5.67	-4.54
	Si	-8.35	-6.88	-5.69	-4.44
	Ca	-9.59	-8.08	-6.90	-6.34
	Fe	-8.54	-6.98	-5.79	-5.01
20000 K	He	-8.73	-5.91	> -4.62	> -4.04
	O	-8.11	-6.55	-5.36	-4.92
	Mg	-8.39	-7.02	-5.86	-4.67
	Si	-8.42	-7.04	-5.88	-4.57
	Ca	-9.66	-8.21	-7.07	-6.51
	Fe	-8.62	-7.11	-5.97	-5.15
25000 K	He	-8.40	-5.80	> -4.70	> -3.91
	O	-8.22	-6.68	-5.55	-4.23
	Mg	-8.47	-7.22	-6.07	-4.72
	Si	-8.51	-7.24	-6.09	-4.75
	Ca	-9.76	-8.38	-7.28	-5.93
	Fe	-8.70	-7.28	-6.18	-4.82

Table 7. Same as Table 4 for models with $M_{\text{H}} = 10^{-10} M_{\odot}$

		10^6 g s^{-1}	10^8 g s^{-1}	10^{10} g s^{-1}
10000 K	He	-7.59	-6.35	-4.49
	O	-8.31	-6.47	-4.87
	Mg	-8.60	-6.68	-4.94
	Si	-8.55	-6.71	-4.97
	Ca	-9.88	-8.03	-6.37
	Fe	-8.80	-6.94	-5.23
10500 K	He	-8.31	-6.30	-4.49
	O	-8.28	-6.48	-4.83
	Mg	-8.58	-6.70	-4.95
	Si	-8.50	-6.66	-4.86
	Ca	-9.86	-8.05	-6.38
	Fe	-8.78	-6.96	-5.24
11000 K	He	-8.76	-6.54	-4.50
	O	-8.55	-6.80	-4.86
	Mg	-8.86	-7.02	-5.17
	Si	-8.70	-6.88	-4.98
	Ca	-10.16	-8.37	-6.48
	Fe	-9.07	-7.28	-5.36
11500 K	He	-8.21	-5.98	-4.15
	O	-8.03	-6.24	-4.50
	Mg	-8.34	-6.48	-4.69
	Si	-8.24	-6.48	-4.76
	Ca	-9.59	-7.75	-6.06
	Fe	-8.51	-6.71	-5.02
12000 K	He	-9.68	-6.96	-3.74
	O	-9.76	-7.87	-4.27
	Mg	-9.21	-7.17	-4.65
	Si	-9.16	-7.17	-4.68
	Ca	-10.95	-8.98	-5.90
	Fe	-9.75	-7.82	-4.81
16000 K	He	-9.55	-7.04	-3.45
	O	-9.73	-7.59	-4.26
	Mg	-9.40	-7.22	-4.65
	Si	-9.16	-7.04	-4.67
	Ca	-11.33	-9.15	-5.89
	Fe	-10.19	-8.02	-4.82
20000 K	He	-9.56	-6.93	-3.38
	O	-9.75	-7.60	-4.29
	Mg	-9.40	-7.22	-4.73
	Si	-9.12	-6.99	-4.70
	Ca	-11.34	-9.16	-5.93
	Fe	-10.20	-8.03	-4.85
25000 K	He	-9.35	-5.68	-3.38
	O	-9.76	-5.94	-4.31
	Mg	-9.41	-6.14	-4.74
	Si	-9.03	-6.22	-4.73
	Ca	-11.35	-7.44	-5.98
	Fe	-10.20	-6.46	-4.82

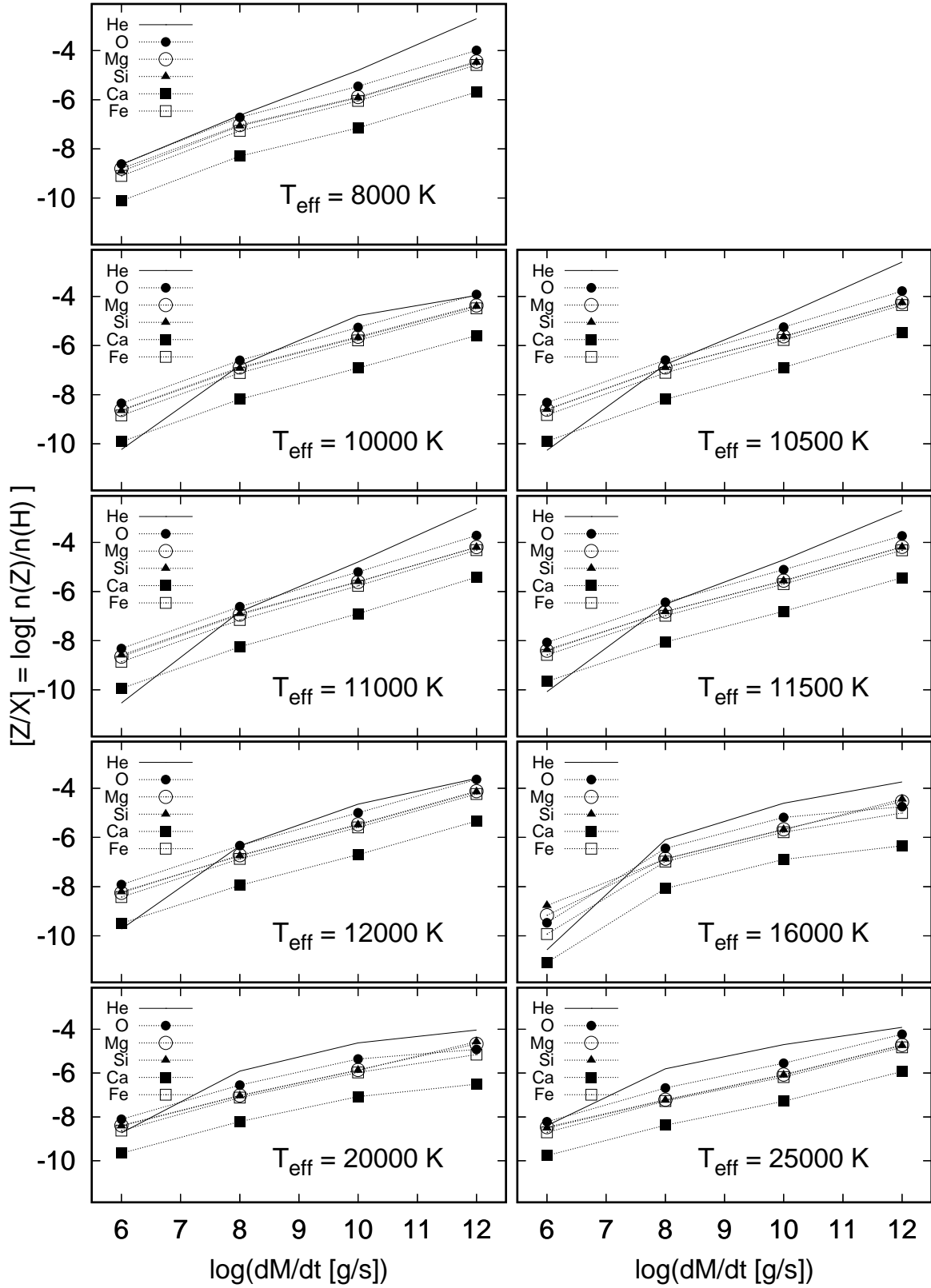


Fig. 12. Same as Figure 10 for models with $M_{\text{H}} = 10^{-8} M_{\odot}$.

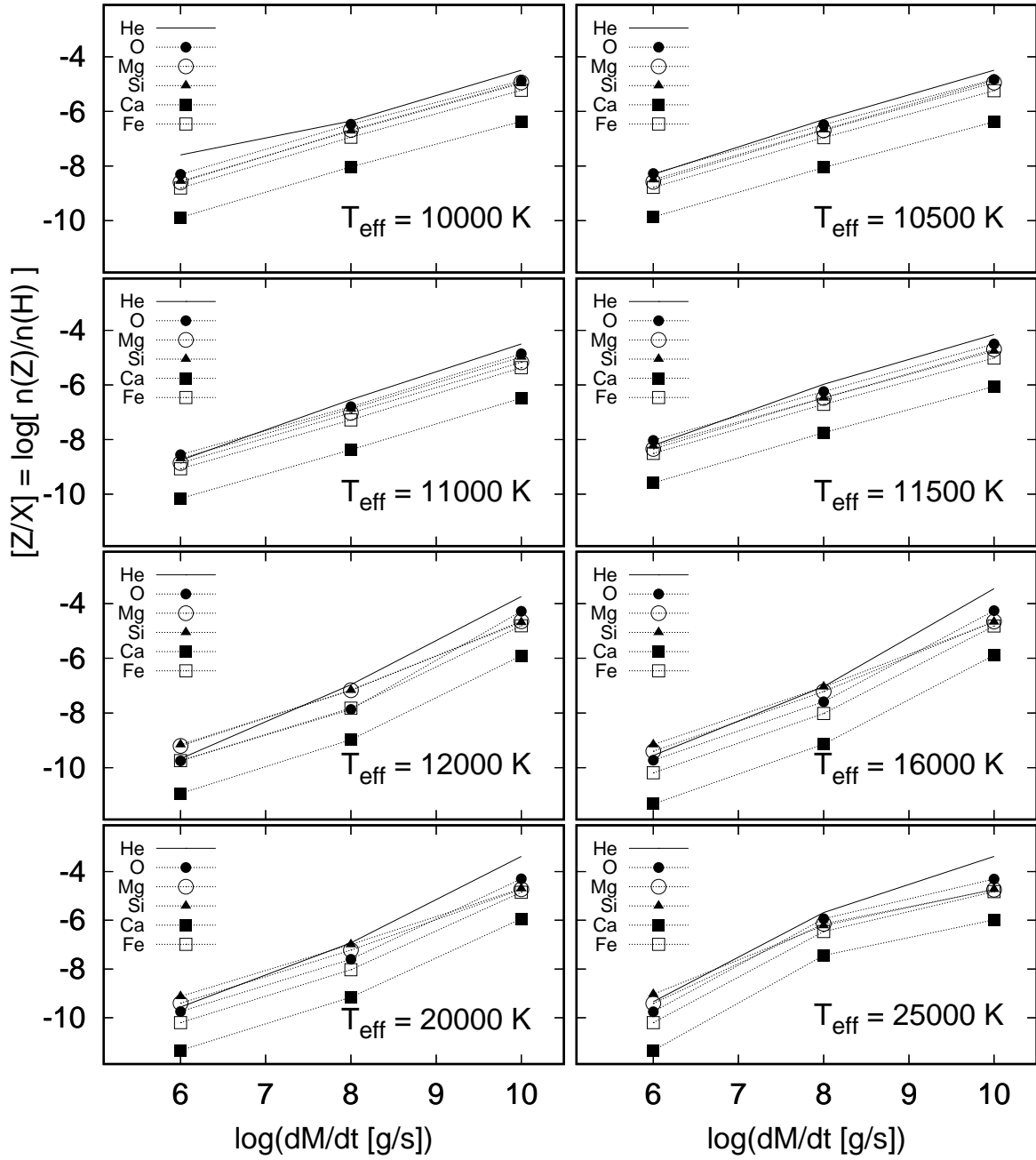


Fig. 13. Same as Figure 10 for models with $M_{\text{H}} = 10^{-10} M_{\odot}$.